Ceramics International 49 (2023) 10499–10505

Contents lists available at ScienceDirect

Ceramics International

journal homepage: www.elsevier.com/locate/ceramint

Simultaneous improvement of coercivity and saturation magnetization of M-type strontium ferrite by Nd^{3+}-Co^{2+} unequal co-substitution

Xiang Yu [a,b], Lichen Wang [b,c], Ruoshui Liu [a,b,d], Ningfang Zhou [b], Zhiyi Xu [a,b], Huayang Gong [b], Tongyun Zhao [a,b], Jirong Sun [a], Fengxia Hu [a], Baogen Shen [a,b,c,d,*]

[a] Beijing National Laboratory for Condensed Matter Physics, Institute of Physics, Chinese Academy of Sciences, Beijing, 100190, China
[b] Ganjiang Innovation Academy, Chinese Academy of Sciences, Ganzhou, Jiangxi, 341119, China
[c] Ningbo Institute of Materials Technology & Engineering, Chinese Academy of Sciences, Ningbo, Zhejiang, 315201, China
[d] School of Rare Earths, University of Science and Technology of China, Hefei, Anhui, 230026, China

ARTICLE INFO

Keywords:
M-type strontium ferrite
Unequal co-substitution
Saturation magnetization
Coercivity
Ion occupancy

ABSTRACT

We synthesized $Sr_{1-x}Nd_xFe_{12-y}Co_yO_{19}$ (x = 0–0.25, y = 0–0.1) using a conventional ceramic route. The crystal structures were analyzed using X-ray diffraction. With increasing Nd^{3+} and Co^{2+} contents, lattice constant a increases, while lattice constant c decreases. In terms of magnetic properties, the saturation magnetization and coercivity are simultaneously increased when $x = y = 0.1$ (equal co-substitution). This is mainly because the bivalent Co^{2+} has a smaller magnetic moment and unquenched orbital moments. When substitution amount x is further increased (unequal co-substitution), the magnetic properties are further improved and reach the optimum values of M_s = 76.4 emu/g and H_c = 5115 Oe owing to the occupation of the 2a site by divalent Fe^{2+}. The occupancies of Co^{2+} and Fe^{2+} are further verified using Raman spectroscopy.

1. Introduction

Rare-earth permanent magnets represented by Nd-Fe-B magnets are the best permanent magnets available at present, and their sales account for approximately 80% of the total permanent magnet market [1]. These magnets are widely used in fields such as wind power generation, new energy vehicles, and electronic equipment. Although rare-earth magnets have a high maximum energy product (BH_{max}), their application is limited by their high cost and supply risk [2,3]. The main alternative in the permanent magnet market is M-type strontium ferrite ($SrFe_{12}O_{19}$, SrM) owing to its low cost, high coercivity (H_c), moderate saturation magnetization (M_s), and corrosion resistance. The annual output of SrM in the permanent magnet market can reach 800 kilotons, making it the permanent magnet material with the largest sales volume [4]. As a magnetic ceramic material, M-type ferrite can be synthesized by the conventional ceramic route [5], sol-gel method [6], and hydrothermal method [7]. It is widely used in permanent magnets [8], magnetic recording [9], and microwave absorption [10,11]. Therefore, the effective enhancement of the magnetic properties of SrM is a research topic of considerable interest. SrM is a typical hexagonal ferrite, in which Fe^{3+} occupies five sites: octahedral sites 2a, 12k, and 4f_2; tetrahedral site 4f_1; and trigonal bipyramid site 2b. From the perspective of the magnetic structure, Fe^{3+} has a majority spin direction in the 2a, 2b, and 12k sites, whereas Fe^{3+} has a minority spin direction in the 4f_1 and 4f_2 sites [12]. As the magnetic properties of SrM are closely related to the presence of Fe^{3+} at different sites, ion substitution is one of the most effective methods for altering the magnetic properties.

La^{3+}–Co^{2+} co-substitution is a common method for improving the magnetic properties of SrM. To ensure the valence balance of the compound, it is generally necessary to carry out equal La^{3+}–Co^{2+} co-substitution (i.e., the substitution amount of La^{3+} is equal to that of Co^{2+}). Iida et al. determined that equal La^{3+}–Co^{2+} co-substitution of 0.3 yielded optimal magnetic properties, including a remanence B_r = 4450 Gs and intrinsic coercivity H_{cj} = 4820 Oe [13]. Sakai et al. performed nuclear magnetic resonance investigations and found that Co^{2+} is mainly present in the 4f_1 site with a minority spin direction and has a small orbital moment. Because the spin magnetic moment of Co^{2+} (3μ_B) is lower than that of Fe^{3+} (5μ_B), M_s will increase slightly. In contrast, Co^{2+} has unquenched orbital moments, and thus it has a higher magnetic anisotropy than Fe^{3+} [14]. In addition, some researchers have also investigated equal co-substitution of other pairs, such as La^{3+}–Mn^{2+} [15], Ce^{3+}–Co^{2+} [16], and Nd^{3+}–Zn^{2+} [17], all of which have yielded

* Corresponding author. Beijing National Laboratory for Condensed Matter Physics, Institute of Physics, Chinese Academy of Sciences, Beijing, 100190, China.
E-mail address: shenbg@iphy.ac.cn (B. Shen).

https://doi.org/10.1016/j.ceramint.2022.11.235
Received 23 September 2022; Received in revised form 11 November 2022; Accepted 18 November 2022
Available online 20 November 2022

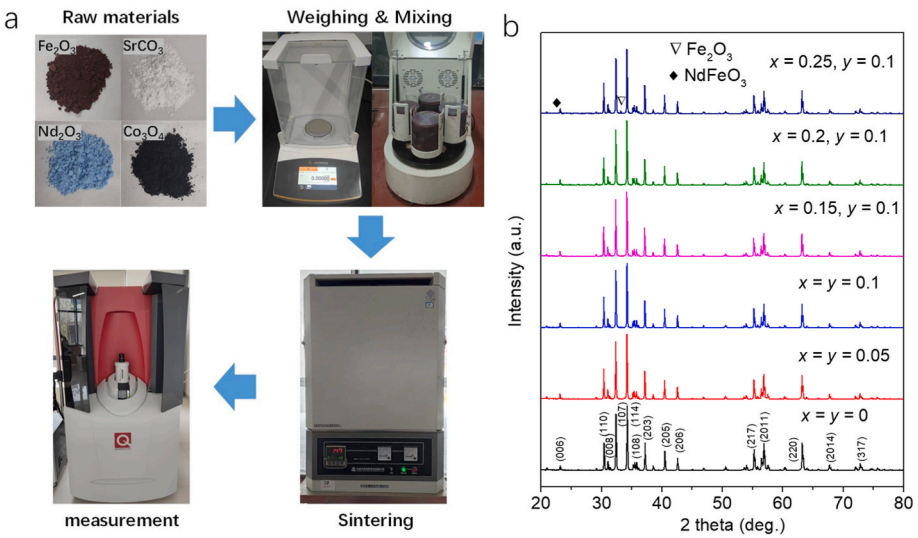

Fig. 1. (a) Synthesis and analysis of $Sr_{1-x}Nd_xFe_{12-y}Co_yO_{19}$. (b) X-ray diffraction patterns of $Sr_{1-x}Nd_xFe_{12-y}Co_yO_{19}$ (x = 0–0.25, y = 0–0.1).

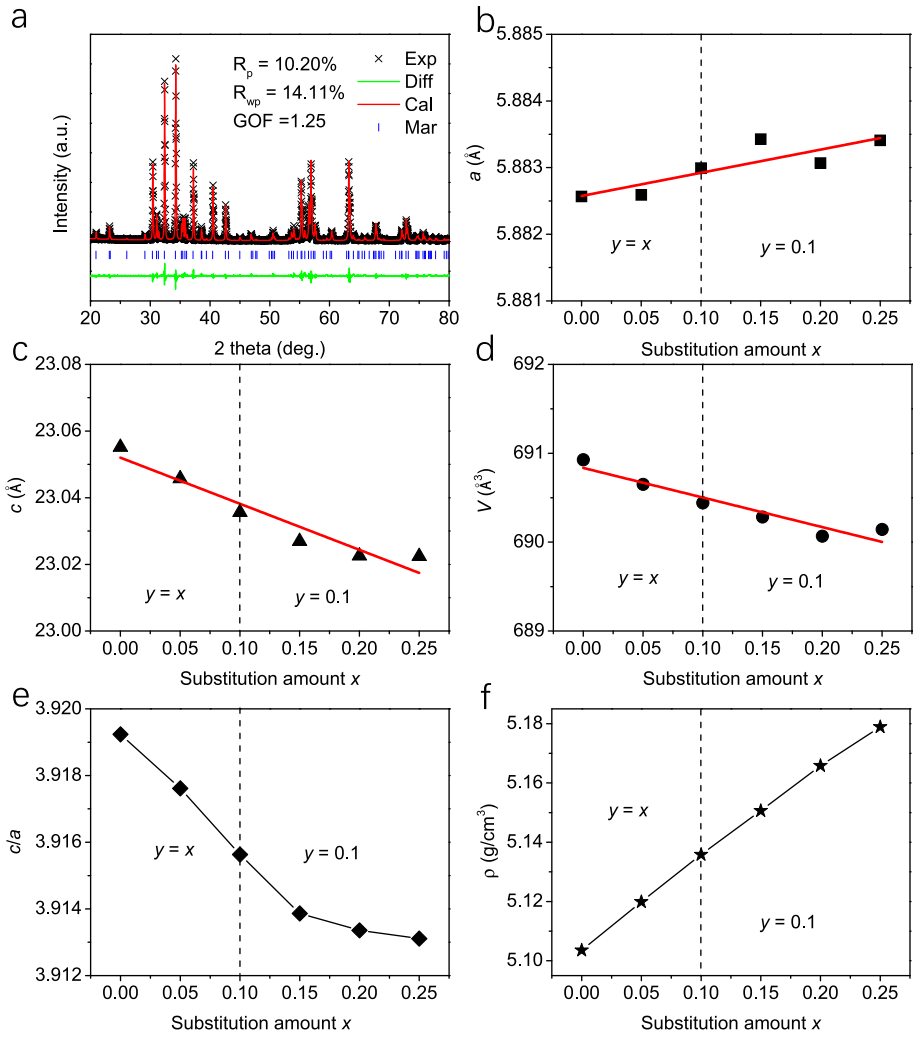

Fig. 2. (a) Refined X-ray diffraction pattern of the sample with $x = y = 0$. Variations in (b) lattice constant a, (c) lattice constant c, (d) V_{cell}, and (e) c/a. (f) XRD density of $Sr_{1-x}Nd_xFe_{12-y}Co_yO_{19}$ (x = 0–0.25, y = 0–0.1).

beneficial results.

Researchers have found that substituting only La^{3+} for Sr^{2+} will cause some trivalent Fe^{3+} to be converted to divalent Fe^{2+}. In this case, the magnetic anisotropy will increase because Fe^{2+} with higher magnetic anisotropy occupies the 2*a* site [18–20]. Liu et al. found that the Sr^{2+} in SrM was partially substituted by La^{3+}, and the optimal magnetic properties of $M_s = 74.1$ Am^2/kg and $H_c = 498.4$ kA/m were at an La^{3+} substitution of 0.15 [21]. Wang et al. reported similar results. When La^{3+} alone substituted for Sr^{2+} in SrM, the maximum H_c of 5960.2 Oe was obtained at an La^{3+} substitution of 0.25, representing an increase in H_c of nearly 50% compared with the non-substituted SrM [22]. Therefore, if the substitution of rare-earth ions is increased to exceed that of Co^{2+} in rare earth–Co^{2+} equal co-substitution, it is possible that the two substitution forms of rare earth–Co^{2+} and rare earth–Fe^{2+} will synergistically enhance the magnetic properties of SrM.

In this study, we prepared $Sr_{1-x}Nd_xFe_{12-y}Co_yO_{19}$ (x = 0–0.25, y = 0–0.1) via the conventional ceramic route. The X-ray diffraction (XRD) results showed that the lattice constant *a* increased slightly with increasing substitution amount, while the lattice constant *c* decreased. Room-temperature magnetic measurements showed that Nd^{3+}–Co^{2+} equal co-substitution ($x \leq 0.1$) could simultaneously enhance the M_s and H_c of the samples, particularly H_c. After further increasing the substitution amount of Nd^{3+}, the magnetic properties of the samples could be further improved to obtain the optimal magnetic properties ($M_s = 76.4$ emu/g, $H_c = 5115$ Oe). This was mainly due to the contributions of divalent Co^{2+} and Fe^{2+}. This material is expected to be a promising candidate for high-performance ferrite permanent magnet.

2. Experimental

2.1. Materials and synthesis

$Sr_{1-x}Nd_xFe_{12-y}Co_yO_{19}$ (x = 0–0.25, y = 0–0.1) samples were synthesized via the conventional ceramic route. High-purity Fe_2O_3 (Aladdin, 99.9%), $SrCO_3$ (Aladdin, 99.95%), Nd_2O_3 (Aladdin, 99.99%), and Co_3O_4 (Aladdin, 99.9%) were fully mixed for 3 h in a planetary ball mill mechanism (Nanjing Boyuntong Instrument, XGB4) with agate balls of diameters 20 mm, 10 mm, and 6 mm; the ball-to-powder weight ratio was 20:1. The (Fe + Co)/(Sr + Nd) atomic ratio was 11.6 in all of the raw material mixtures. After drying the wet powder in a drying oven, it was sintered at 1250 °C for 40 min to obtain $Sr_{1-x}Nd_xFe_{12-y}Co_yO_{19}$ samples.

Based on the concept described in the introduction, for the $Sr_{1-x}Nd_xFe_{12-y}Co_yO_{19}$ (x = 0–0.25, y = 0–0.1) samples, we first prepared Nd^{3+}–Co^{2+} equally co-substituted samples ($x = y = 0.05$ and $x = y = 0.1$) to improve the magnetic properties by the introduction of bivalent Co^{2+}. We then increased the amount of Nd^{3+} substitution with a fixed Co^{2+} substitution of 0.1 (x = 0.15, 0.2, 0.25 and y = 0.1) to obtain Nd^{3+}–Co^{2+} unequally co-substituted samples and further improve the magnetic properties of the sample through the introduction of bivalent Fe^{2+}.

2.2. Characterization

The crystal structures of the samples were characterized by XRD (BRUKE D8 ADVANCE) with Cu Kα radiation (λ = 1.54184 Å), and the lattice parameters and phase compositions were obtained through refinement of the XRD data. Micro-Raman spectroscopy (RENUSHAW inVia Raman Microscope) was used to analyze the Raman spectra of the samples. Scanning electron microscopy (SEM; TESCAN CLARA) was used to characterize the size and morphology of the grains. Magnetic hysteresis loops were measured at 300 K using a superconducting quantum interference device magnetometer (SQUID-VSM; Quantum Design). The temperature dependence of the moment (M-T curve) was measured in zero-field cooling (ZFC) mode under a field of 50,000 Oe.

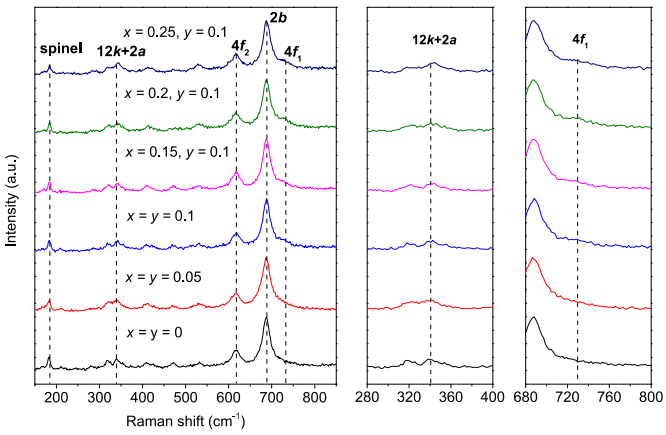

Fig. 3. Raman spectra of $Sr_{1-x}Nd_xFe_{12-y}Co_yO_{19}$ (x = 0–0.25, y = 0–0.1).

3. Results and discussion

The experimental procedure is illustrated in Fig. 1a. All samples were prepared using a conventional ceramic route, and the physical properties of the samples were measured. The phase formation and structural details were obtained using XRD. Fig. 1b shows the XRD patterns of $Sr_{1-x}Nd_xFe_{12-y}Co_yO_{19}$ (x = 0–0.25, y = 0–0.1) calcined at 1250 °C; the results are consistent with the standard card (COD#1008856). Other the sample with x = 0.25 and y = 0.1 containing 2.46% Fe_2O_3 and 0.35% $NdFeO_3$ impurities, the samples all exhibit a single hexagonal structure.

Detailed information regarding the crystal structure of the samples was obtained by refinement of the XRD data using Topas software, and the refinement parameter, R_{wp}, was maintained below 15% to ensure data reliability. Fig. 2a shows the refined XRD patterns of a representative sample ($x = y = 0$, SrM), and the related fitting parameter values are listed ($R_p = 10.20\%$, $R_{wp} = 14.11\%$, GOF = 1.25). The lattice constants, *a* and *c*, and the unit cell volume, V_{cell}, are calculated using Equations (1) and (2), respectively [23,24].

$$d_{hkl} = \sqrt{\frac{4}{3}\frac{h^2 + hk + k^2}{a^2} + \frac{l^2}{c^2}} \quad (1)$$

where d_{hkl} is the interplanar spacing; *h*, *k*, and *l* are the Miller indices of the crystal plane corresponding to the diffraction peak; and *a* and *c* are lattice parameters.

$$V_{cell} = \frac{\sqrt{3}}{2}a^2c \quad (2)$$

where V_{cell} is the cell volume, and *a* and *c* are lattice parameters. Lattice parameter *a* increases with the amount of substitution *x* (Fig. 2b) because the ionic radii of divalent Co^{2+} and Fe^{2+} are larger than that of trivalent Fe^{3+} [25]. For the sample with $x = 0.25$, lattice constant *a* increases by approximately 0.014% compared to that of SrM ($x = 0$). In contrast, lattice constant *c* decreases with increasing *x* (Fig. 2c). The value of *c* is 23.0224 Å at $x = 0.25$, which is approximately 0.142% lower than that of SrM ($x = 0$). The change in the value of *c* is mainly due to the substitution of Sr^{2+} by Nd^{3+}, which has a smaller ionic radius [25]. The contraction of the local dodeca-coordinated SrO_{12} causes compression of the lattice along the *c*-axis [26]. As a result of the variations in lattice constants *a* and *c*, the cell volume, V_{cell}, decreases with increasing *x*; the maximum decrease of 0.113% occurs at $x = 0.25$ (Fig. 2d). All of the samples have a typical M-type magnetoplumbite structure because *c*/*a* is less than 3.98 [27], as shown in Fig. 2e. The XRD density (ρ) can be calculated using Equation (3) [28,29]:

$$\rho = \frac{2M}{N_A V_{cell}} \quad (3)$$

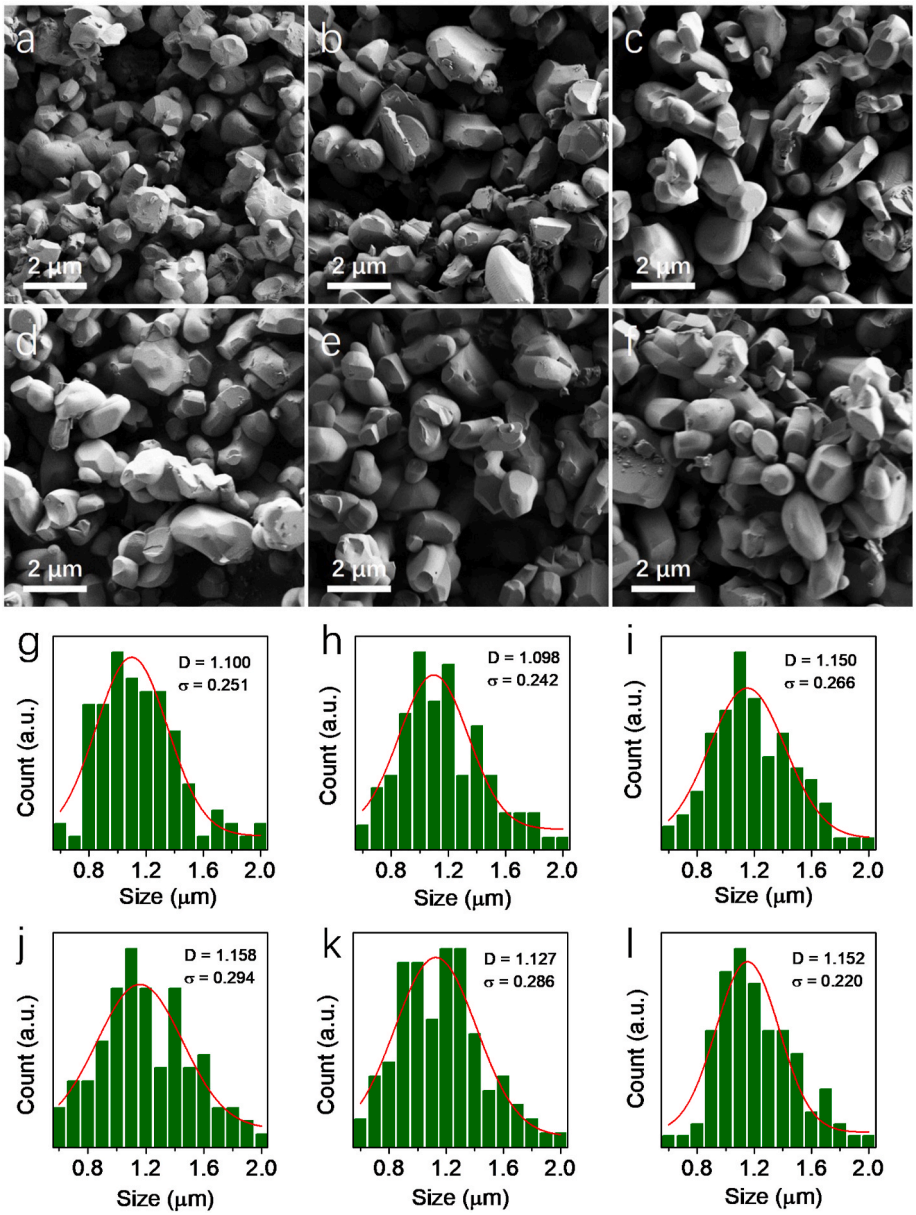

Fig. 4. Scanning electron microscopy images and size distribution of $Sr_{1-x}Nd_xFe_{12-y}Co_yO_{19}$: (a) (g) $x = y = 0$; (b) (h) $x = y = 0.05$; (c) (i) $x = y = 0.1$; (d) (j) $x = 0.15$, $y = 0.1$; (e) (k) $x = 0.2$, $y = 0.1$; (f) (l) $x = 0.25$, $y = 0.1$.

where M is the molar mass of the sample, N_A is Avogadro's number, and V_{cell} is the cell volume. As shown in Fig. 2f, the sample density increases with increasing substitution. This is due to the gradual decrease in the cell volume with increasing Nd^{3+} content. In contrast, the masses of Nd^{3+} ($m_{Nd} = 144.24$) and Co^{2+} ($m_{Fe} = 58.93$) are larger than those of Sr^{2+} ($m_{Sr} = 87.62$) and Fe^{3+} ($m_{Fe} = 55.84$), respectively. The increase in density will increase the volume magnetization of the material, which is desirable for permanent magnets.

The dynamic behavior of cations at various sites and their distribution was investigated using Raman spectroscopy. For typical SrM, there are a total of 64 ions in a unit cell, of which 24 Fe^{3+} ions are distributed in tetrahedral sites (FeO_4), bipyramidal sites (FeO_5), and octahedral sites (FeO_6). Group theory predicts that SrM will have 42 Raman active modes: $\Gamma_{raman} = 11A_{1g} + 14E_{1g} + 17E_{2g}$ [30]. As shown in Fig. 3, room-temperature Raman spectra of $Sr_{1-x}Nd_xFe_{12-y}Co_yO_{19}$ ($x = 0$–0.25, $y = 0$–0.1) were obtained in the range of 150–850 cm^{-1}. Based on results in the literature, the characteristic Raman peaks can be assigned to different vibrational modes. The band at 729 cm^{-1} is attributed to the tetrahedral site (FeO_4, $4f_1$ site) with A_{1g} symmetry. The bands at 686 cm^{-1} and 615 cm^{-1} are assigned to the bipyramidal (FeO_5, $2b$ site) and octahedral sites (FeO_6, $4f_2$ site), respectively, both with A_{1g} symmetry. The band at 410 cm^{-1} is attributed to the $12k$ site (octahedral FeO_6) with A_{1g} symmetry, whereas the bands at 470 cm^{-1} and 341 cm^{-1} are attributed to the mixed octahedral FeO_6 ($12k$ and $2a$ sites) with A_{1g} symmetry. The band at 319 cm^{-1} belongs to the E_{2g} symmetry group. The bands at 530, 281, 210, 181, and 168 cm^{-1} are assigned E_{1g} symmetry, while the bands at 181 cm^{-1} and 168 cm^{-1} are attributed to the entire spinel block [30–32].

The mass and force constant affect the shift of the peaks in the Raman spectra. The substitution of other ions for the original Fe^{3+} in SrM will lead to changes in the ion mass and force constants (based on the bond length, lattice parameters, covalency, etc.) [33]. Therefore, information regarding the ion distribution can be obtained from the changes in the Raman spectra. There is a broadening and slight shift to a lower wavenumber of the band at 729 cm^{-1} (tetrahedra, $4f_1$ site). Because the mass of Co^{2+} ($m_{Fe} = 58.93$) is slightly heavier than that of Fe^{3+} ($m_{Fe} = 55.84$),

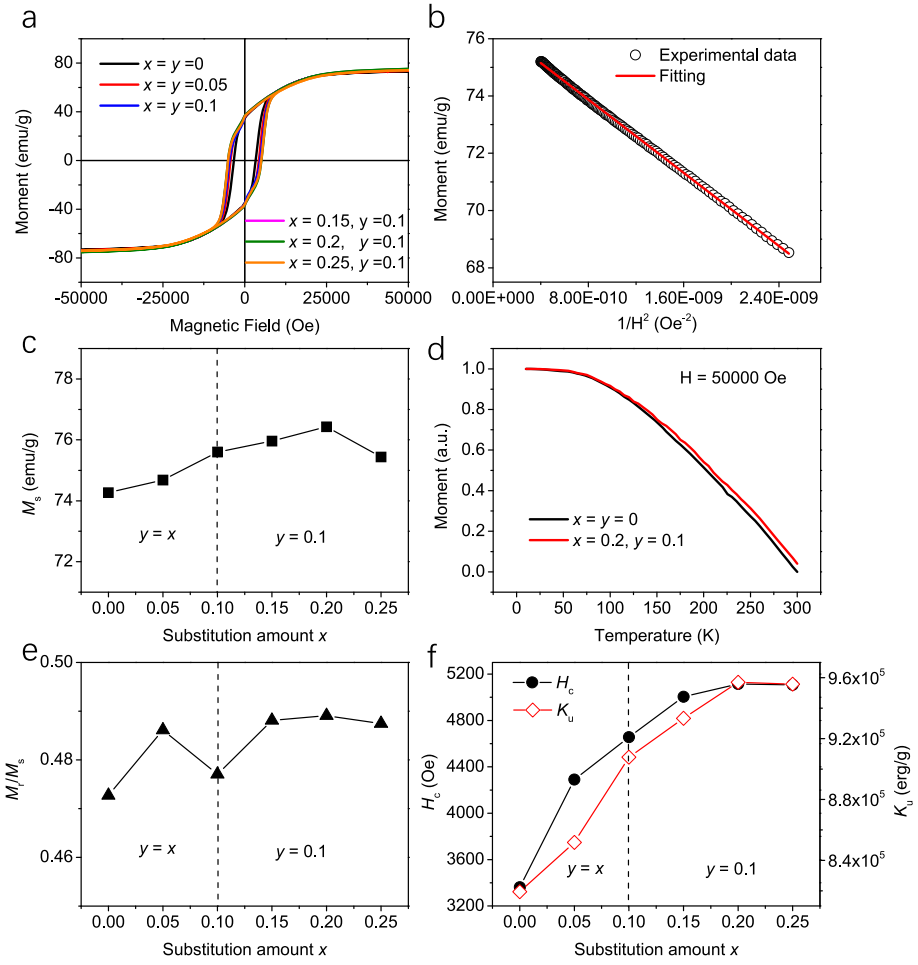

Fig. 5. (a) Hysteresis loops of $Sr_{1-x}Nd_xFe_{12-y}Co_yO_{19}$ (x = 0–0.25, y = 0–0.1). (b) Experimental and fitted moment versus $1/H^2$ curves in the range of 20,000 Oe to 50,000 Oe for the sample with $x = 0.2$, $y = 0.1$. (c) Variation in M_s for $Sr_{1-x}Nd_xFe_{12-y}Co_yO_{19}$ (x = 0–0.25, y = 0–0.1). (d) M-T curves of the samples with $x = y = 0$ and $x = 0.2$, $y = 0.1$. (e) M_r/M_s, (f) H_c and K_u for $Sr_{1-x}Nd_xFe_{12-y}Co_yO_{19}$ (x = 0–0.25, y = 0–0.1).

a slight shift of the Raman peak to lower wavenumbers will occur. On the other hand, the ionic radius of Co^{2+} (0.75 Å) is larger than that of Fe^{3+} (0.64 Å), and thus the substitution of Co^{2+} for Fe^{3+} will lead to distortion of the local tetrahedron, causing broadening of the Raman peak corresponding to this position. As the substitution amount x increases from 0 to 0.1, a shift and broadening of the Raman peak can be observed, whereas this Raman peak does not change when x is further increased from 0.1 to 0.25. This is mainly because the Co^{2+} substitution amount, y, was maintained at 0.1 as x was varied from 0.1 to 0.25. Combined with the relevant results in the literature, it can be inferred that Co^{2+} in our sample can occupy the $4f_1$ site [14].

Next, we examine the band at 341 cm^{-1}, which is associated with the mixed octahedral FeO_6 (12k and 2a sites). When the substitution x ranges from 0 to 0.15, the Raman peak exhibits no obvious change, whereas when x is increased from 0.2 to 0.25, the Raman peak is shifted to a higher wavenumber with slight broadening. This is mainly because when the substitution amount of Nd^{3+} is higher than that of Co^{2+}, part of the trivalent Fe^{3+} will be converted to divalent Fe^{2+}. The difference in mass between divalent Fe^{2+} and trivalent Fe^{3+} is negligible, and thus the shift of the Raman peak is mainly caused by the change in the force constant [33]. According to the literature, the resultant divalent Fe^{2+} occupies the 2a site [34]. The variation in this Raman peak indicates that the divalent Fe^{2+} in our sample should occupy the 2a site.

The Raman peaks at 686 cm^{-1} and 615 cm^{-1} represent the bipyramidal and octahedral vibration modes, respectively. It can be observed that neither of these peaks change with the increase in substitution amount, x, which indicates that neither Co^{2+} nor Fe^{2+} occupy the $4f_2$ or 2b sites. The Raman peak at 181 cm^{-1} also does not change with increasing x. This result shows that a small amount of Nd^{3+}–Co^{2+} co-substitution has no obvious influence on the vibration mode of the entire spinel block.

Table 1
Values of M_s, M_r/M_s, H_c, and K_u for $Sr_{1-x}Nd_xFe_{12-y}Co_yO_{19}$ (x = 0–0.25, y = 0–0.1).

x	M_s (emu/g)	M_r/M_s	H_c (Oe)	K_u (× 10^5 erg/g)
0	74.2	0.472	3363	8.193
0.05	74.6	0.486	4290	8.517
0.1	75.6	0.477	4656	9.077
0.15	75.9	0.488	5005	9.333
0.2	76.4	0.489	5115	9.570
0.25	75.4	0.487	5107	9.557

The micromorphology of $Sr_{1-x}Nd_xFe_{12-y}Co_yO_{19}$ (x = 0–0.25, y = 0–0.1) is shown in Fig. 4a–f with a magnification of 20k and a scale bar of 2 μm. All of the samples exhibit similar granular morphology, which indicates that a small amount of Nd^{3+}–Co^{2+} co-substitution has little effect on the grain formation process. The grain sizes of all samples are approximately 1 μm, as counted using the Nano Measurer software (Fig. 4g–l). Because the grain size is closely related to the sintering temperature and time, controlling the relevant parameters to obtain particles close to the single-domain size can help optimize the magnetic properties of the samples.

The hysteresis loops of $Sr_{1-x}Nd_xFe_{12-y}Co_yO_{19}$ (x = 0–0.25, y = 0–0.1)

were measured at 300 K in an applied field range of −50,000 Oe to 50,000 Oe (Fig. 5a), and the relevant magnetic parameters are listed in Table 1. It can be seen that Nd^{3+}–Co^{2+} co-substitution affects the magnetic properties of SrM. According to the Stoner–Wohlfarth approximation, M_s values were obtained via the law of approaching saturation (Fig. 5b). This can be described by Equation (4) in the high-field region [35,36]:

$$M = M_s\left[1 - \frac{\beta}{H^2}\right] \tag{4}$$

where β is a parameter related to the magnetic anisotropy. When $1/H^2 = 0$, M_s can be obtained by fitting a curve. The value of β can then be obtained from the slope of the fitted curve. As shown in Fig. 5c, M_s initially increases slightly from 74.2 emu/g ($x = 0$) to 75.6 emu/g ($x = 0.1$), then increases to 76.4 emu/g ($x = 0.2$), and finally decreases to 75.4 emu/g ($x = 0.25$). For the sample with $x = 0.1$, the increase in M_s is due to Co^{2+} with a smaller magnetic moment occupying the $4f_1$ site. The electron configurations of Fe^{3+} and Co^{2+} are d^5 and d^7, respectively, and the corresponding spin magnetic moments are 5 μ_B and 3 μ_B, respectively. Co^{2+}, with a lower magnetic moment, occupies the site with a minority spin direction, which will increase M_s. For the samples with x from 0.1 to 0.2, M_s decreases with an increase in the substitution amount because divalent Fe^{2+} with a lower magnetic moment (4 μ_B) occupies the 2a site (majority spin direction).

However, an increase in M_s of the samples with increasing substitution is observed, mainly because of the temperature dependence of M_s. According to the mean-field theory, the magnetization of small spin quantum numbers has a weaker temperature dependence than that of large spin quantum numbers. Therefore, thermal agitation has less influence on the magnetization of divalent Fe^{2+}. In other words, M_s should decrease with an increase in divalent Fe^{2+} at low temperatures, whereas M_s increases relatively at room temperature because divalent Fe^{2+} is less affected by thermal agitation [37] (Fig. 5d). In addition, the magnetic moment of Nd^{3+} is 3.5 μ_B, making it a substitute for the non-magnetic Sr^{2+}, which should increase the M_s of the sample [38]. Finally, the decrease in M_s of the sample with $x = 0.25$ and $y = 0.1$ occurs because the sample contains 2.46% antiferromagnetic Fe_2O_3.

According to the Stoner–Wohlfarth theory, an M_r/M_s value of 0.83 corresponds to cubic anisotropy, while M_r/M_s of around 0.5 indicates uniaxial anisotropy [39]. As shown in Fig. 5e, the M_r/M_s values of all samples are between 0.47 and 0.49, which indicates that the preferred magnetization axis of all samples is along the crystal c-axis.

As shown in Fig. 5f, H_c increases monotonically with an increase in the Nd^{3+}–Co^{2+} co-substitution amount. H_c initially increases from 3363 Oe ($x = 0$) to 4656 Oe ($x = 0.1$), then increases to 5115 Oe ($x = 0.2$), and finally remains at 5107 Oe ($x = 0.25$). Owing to the small amount of Nd^{3+}–Co^{2+} co-substitution, the particle size remains basically unchanged, as shown in the SEM images. Therefore, the variation in H_c caused by the change in size can be neglected, and the reason for the variation in H_c is thus the change in magnetic anisotropy. The magnetic anisotropy constant (K_u) can be calculated using Equation (5) [35,36]:

$$K_u = M_s\sqrt{\frac{15\beta}{4}} \tag{5}$$

where the value of β can be calculated using Equation (4). It can be observed that the variation in K_u is similar to the variation in H_c in Fig. 5f. With an increase in x, K_u increases correspondingly. For the sample with $x = y = 0.1$, K_u reaches 9.077×10^5 erg/g, and the increase in K_u is mainly due to the unquenched orbital moments of the bivalent Co^{2+}. When x is further increased while y is constant at 0.1, the K_u of the sample ($x = 0.25$, $y = 0.1$) further increases to 9.557×10^5 erg/g. The further improvement in K_u is attributed to the spin-orbit interaction of the bivalent Fe^{2+} [40].

4. Conclusion

In this study, we investigate Nd^{3+}–Co^{2+} co-substituted SrM. As the amount of Nd^{3+}–Co^{2+} substitution increases, lattice constant a increases slightly, whereas lattice constant c decreases. Magnetic measurements at room temperature show that when the substitution amount is $x = y \leq 0.1$, M_s and H_c are enhanced simultaneously. When the substitution amount of Nd^{3+} is further increased and that of Co^{2+} is constant at 0.1, the sample ($x = 0.2$, $y = 0.1$) with the optimal magnetic properties can be obtained ($M_s = 76.4$ emu/g, $H_c = 5115$ Oe). This is mainly due to the contributions of the Co^{2+} occupying the $4f_1$ site and Fe^{2+} occupying the 2a site to the magnetic properties. This material is expected to be a promising candidate for high-performance ferrite permanent magnets, and this ion substitution strategy is expected to be extended, such as in La^{3+}–Co^{2+}, Ce^{3+}–Co^{2+}, and Pr^{3+}–Co^{2+} substitution.

Declaration of competing interest

The authors declare that they have no known competing financial interests or personal relationships that could have appeared to influence the work reported in this paper.

Acknowledgments

This work was supported by the Science Center of the National Science Foundation of China (52088101), the National Key Research and Development Program of China (2021YFB3501202, 2020YFA0711502, 2019YFA0704900, 2018YFA0305704), the National Natural Sciences Foundation of China (U1832219, 51971240, 52101228, 52001012), the Strategic Priority Research Program B (XDB33030200), Beijing Natural Science Foundation (2214070) and the key program of the Chinese Academy of Sciences (ZDRW-CN-2021-3), the Research Projects of Ganjiang Innovation Academy, Chinese Academy of Sciences (E055ZA01).

References

[1] J.C. Guzmán-Mínguez, L. Moreno-Arche, C. Granados-Miralles, J. López-Sánchez, P. Marín, J.F. Fernández, A. Quesada, Boosting the coercivity of $SrFe_{12}O_{19}$ nanocrystalline powders obtained using the citrate combustion synthesis method, J. Phys. D Appl. Phys. 54 (2020), 014002.
[2] L.H. Lewis, F. Jiménez-Villacorta, Perspectives on permanent magnetic materials for energy conversion and power generation, Metall. Mater. Trans. A 44 (2013) 2–20.
[3] J.M.D. Coey, Permanent magnets: plugging the gap, Scripta Mater. 67 (2012) 524–529.
[4] J.C. Guzmán-Mínguez, V. Fuertes, C. Granados-Miralles, J.F. Fernández, A. Quesada, Greener processing of $SrFe_{12}O_{19}$ ceramic permanent magnets by two-step sintering, Ceram. Int. 47 (2021) 31765–31771.
[5] S. Sung-Woo, K. Bu-An, K. Hae-Woong, L. Jung-Goo, Synthesis and magnetic properties of Na-La-Co system M-type ferrite, Journal of Magnetics 26 (2021) 305–310.
[6] S. Younus, G. Murtaza, N.M. Aloufi, H.H. Somaily, Structural, dielectric, and magnetic properties of Pr–Cr co-doped $Pr_xBa_{1-x}Cr_yFe_{12-y}O_{19}$ barium hexaferrites, Ceram. Int. 48 (2022) 31041–31053.
[7] S. Dong, C. Lin, X. Meng, One-pot synthesis and microwave absorbing properties of ultrathin $SrFe_{12}O_{19}$ nanosheets, J. Alloys Compd. 783 (2019) 779–784.
[8] S. Kumar Godara, Nomita, V. Kaur, A.K. Srivastava, D. Basandrai, J. Ahmed, J. Mohammed, M. Singh, P. Kaur, A. Mehtab, T. Ahmad, R, Dhaka Kumar, P. K. Maji, A. Kumar Sood, Effect on Magnetic, morphological and structural properties of Zn^{2+}-Zr^{4+} substituted SrM for permanent magnet based appliances, J. Magn. Magn Mater. 560 (2022), 169626.
[9] N. Yasmin, S. Abdulsatar, M. Hashim, M. Zahid, S. Fatima Gillani, A. Kalsoom, M. Naeem Ashiq, I. Inam, M. Safdar, M. Mirza, Structural and magnetic studies of Ce-Mn doped M-type $SrFe_{12}O_{19}$ hexagonal ferrites by sol-gel auto-combustion method, J. Magn. Magn Mater. 473 (2019) 464–469.
[10] J. Li, Y. Hong, S. He, W. Li, H. Bai, Y. Xia, G. Sun, Z. Zhou, A neutron diffraction investigation of high valent doped barium ferrite with wideband tunable microwave absorption, Journal of Advanced Ceramics 11 (2022) 263–272.
[11] J. Ma, B. Zhao, H. Xiang, F.-Z. Dai, Y. Liu, R. Zhang, Y. Zhou, High-entropy spinel ferrites MFe_2O_4 (M = Mg, Mn, Fe, Co, Ni, Cu, Zn) with tunable electromagnetic properties and strong microwave absorption, Journal of Advanced Ceramics 11 (2022) 754–768.

[12] C. de Julián Fernández, C. Sangregorio, J. de la Figuera, B. Belec, D. Makovec, A. Quesada, Progress and prospects of hard hexaferrites for permanent magnet applications, J. Phys. D Appl. Phys. 54 (2021), 153001.
[13] K. Iida, Y. Minachi, K. Masuzawa, M. Kawakami, H. Nishio, H. Taguchi, High - performance ferrite magnets: M - type Sr - ferrite containing lanthanum and cobalt, J. Magn. Soc. Jpn. 23 (1999) 1093–1096.
[14] H. Sakai, T. Hattori, Y. Tokunaga, S. Kambe, H. Ueda, Y. Tanioku, C. Michioka, K. Yoshimura, K. Takao, A. Shimoda, T. Waki, Y. Tabata, H. Nakamura, Occupation sites and valence states of Co dopants in (La, Co)-codoped M-type Sr ferrite: ^{57}Fe and ^{59}Co nuclear magnetic resonance studies, Phys. Rev. B 98 (2018), 064403.
[15] Y. Liu, M.G.B. Drew, Y. Liu, J. Wang, M. Zhang, Preparation and magnetic properties of La–Mn and La–Co doped barium hexaferrites prepared via an improved co-precipitation/molten salt method, J. Magn. Magn Mater. 322 (2010) 3342–3345.
[16] M. Shezad, X. Liu, S. Feng, X. Kan, W. Wang, C. Liu, T.J. Shehzad, K.M.U. Rehman, Characterizations analysis of magneto-structural transitions in Ce-Co doped SrM based nano $Sr_{1-x}Ce_xFe_{12-x}Co_xO_{19}$ hexaferrite crystallites prepared by ceramic route, J. Magn. Magn Mater. 497 (2020), 166013.
[17] M.A. Almessiere, Y. Slimani, A. Baykal, Impact of Nd-Zn co-substitution on microstructure and magnetic properties of $SrFe_{12}O_{19}$ nanohexaferrite, Ceram. Int. 45 (2019) 963–969.
[18] F.K. Lotgering, Magnetic anisotropy and saturation of $LaFe_{12}O_{19}$ and some related compounds, J. Phys. Chem. Solid. 35 (1974) 1633–1639.
[19] R. Grössinger, M. Küpferling, M. Haas, H. Müller, G. Wiesinger, C. Ritter, Magnetic anisotropy and magnetostriction of $LaFe_{12}O_{19}$, J. Magn. Magn Mater. 310 (2007) 2587–2589.
[20] M. Küpferling, R. Grössinger, M.W. Pieper, G. Wiesinger, H. Michor, C. Ritter, F. Kubel, Structural phase transition and magnetic anisotropy of La-substituted M-type Sr hexaferrite, Phys. Rev. B 73 (2006), 144408.
[21] X. Liu, W. Zhong, S. Yang, Z. Yu, B. Gu, Y. Du, Structure and magnetic properties of La^{3+}-substituted strontium hexaferrite particles prepared by sol–gel method, phys. stat. solid. (a) 193 (2002) 314–319.
[22] Z. Wang, W. Yang, Z. Zhou, M. Jin, J. Xu, Y. Sui, Preparation and magnetic properties of La-substituted strontium hexaferrite by microwave-assisted sol-gel method, J. Supercond. Nov. Magnetism 29 (2016) 981–984.
[23] C. Liu, X. Kan, F. Hu, X. Liu, S. Feng, J. Hu, W. Wang, K.M. Ur Rehman, M. Shezad, C. Zhang, H. Li, S. Zhou, Q. Wu, Characterizations of magnetic transition behavior and electromagnetic properties of Co-Ti co-substituted SrM-based hexaferrites $SrCo_xTi_xFe_{12-2x}O_{19}$ compounds, J. Alloys Compd. 784 (2019) 1175–1186.
[24] C. Liu, X. Kan, F. Hu, X. Liu, S. Feng, J. Hu, W. Wang, K.M.U. Rehman, M. Shezad, C. Zhang, H. Li, S. Zhou, Q. Wu, Investigations of Ce-Zn co-substitution on crystal structure and ferrimagnetic properties of M-type strontium hexaferrites $Sr_{1-x}Ce_xFe_{12-x}Zn_xO_{19}$ compounds, J. Alloys Compd. 785 (2019) 452–459.
[25] R.D. Shannon, Revised effective ionic radii and systematic studies of interatomic distances in halides and chalcogenides, Acta Crystallogr. A 32 (1976) 751–767.
[26] D. Seifert, J. Töpfer, M. Stadelbauer, R. Grössinger, J.-M. Le Breton, Rare-earth-substituted $Sr_{1-x}Ln_xFe_{12}O_{19}$ hexagonal ferrites, J. Am. Ceram. Soc. 94 (2011) 2109–2118.
[27] T.R. Wagner, Preparation and crystal structure analysis of magnetoplumbite-type $Baga_{12}O_{19}$, J. Solid State Chem. 136 (1998) 120–124.
[28] J. Li, H. Zhang, Y. Liu, Q. Li, T. Zhou, H. Yang, Phase formation, magnetic properties and Raman spectra of Co–Ti co-substitution M-type barium ferrites, Appl. Phys. A 119 (2015) 525–532.
[29] Y. Yang, H. Zhang, J. Li, F. Xu, G. Gan, D. Wen, Effects of Bi_2O_3-Nb_2O_5 additives on microstructure and magnetic properties of low-temperature-fired NiCuZn ferrite ceramics, Ceram. Int. 44 (2018) 10545–10550.
[30] J. Kreisel, G. Lucazeau, H. Vincent, Raman spectra and vibrational analysis of $BaFe_{12}O_{19}$ hexagonal ferrite, J. Solid State Chem. 137 (1998) 127–137.
[31] H.H. Nguyen, W.H. Jeong, T.L. Phan, B.W. Lee, D.S. Yang, N. Tran, N.T. Dang, Coexistence of Zn and Fe ions influenced magnetic and microwave shielding properties of Zn-doped $SrFe_{12}O_{19}$ ferrites, J. Magn. Magn Mater. 537 (2021), 168195.
[32] M.A.P. Buzinaro, M.A. Macêdo, B.F.O. Costa, N.S. Ferreira, Disorder of $Fe^{(2)}O_5$ bipyramids and spin-phonon coupling in $SrFe_{12}O_{19}$ nanoparticles, Ceram. Int. 45 (2019) 13571–13574.
[33] J. Kreisel, G. Lucazeau, H. Vincent, Raman study of substituted barium ferrite single crystals, $BaFe_{12-2x}Me_xCo_xO19$ (Me=Ir, Ti), J. Raman Spectrosc. 30 (1999) 115–120.
[34] V. Chlan, K. Kouřil, K. Uličná, H. Štěpánková, J. Töpfer, D. Seifert, Charge localization and magnetocrystalline anisotropy in La, Pr, and Nd substituted Sr hexaferrites, Phys. Rev. B 92 (2015), 125125.
[35] M.A. Almessiere, Y. Slimani, A. Baykal, Structural and magnetic properties of Ce-doped strontium hexaferrite, Ceram. Int. 44 (2018) 9000–9008.
[36] L.H. Omari, A. Lekdadri, H. Lassri, O. Mentré, C. Minaud, E. Dhahri, C. Jama, Effect of low amount Mn doping on structural and magnetic properties of $SrFe_{12}O_{19}$: effective magnetic anisotropy study by Stoner - wohlfarth model, Mater. Today Commun. 27 (2021), 102257.
[37] H. Ueda, Y. Tanioku, C. Michioka, K. Yoshimura, Magnetocrystalline anisotropy of La- and Co-substituted M-type strontium ferrites: role of Co^{2+} and Fe^{2+}, Phys. Rev. B 95 (2017), 224421.
[38] B.K. Rai, S.R. Mishra, V.V. Nguyen, J.P. Liu, Synthesis and characterization of high coercivity rare-earth ion doped $Sr_{0.9}RE_{0.1}Fe_{10}Al_2O_{19}$ (RE: Y, La, Ce, Pr, Nd, Sm, and Gd), J. Alloys Compd. 550 (2013) 198–203.
[39] E.C. Stoner, E.P. Wohlfarth, A mechanism of magnetic hysteresis in heterogeneous alloys, IEEE Trans. Magn. 27 (1991) 3475–3518.
[40] C. Bhandari, M.E. Flatté, D. Paudyal, Enhanced magnetic anisotropy in lanthanum M-type hexaferrites by quantum-confined charge transfer, Phys. Rev. Mater. 5 (2021), 094415.